Computational Materials Science 201 (2022) 110905

Contents lists available at ScienceDirect

Computational Materials Science

journal homepage: www.elsevier.com/locate/commatsci

Deep learning for mapping element distribution of high-entropy alloys in scanning transmission electron microscopy images

Marco Ragone [a], Mahmoud Tamadoni Saray [a], Lance Long [b], Reza Shahbazian-Yassar [a], Farzad Mashayek [a], Vitaliy Yurkiv [a,*]

[a] Department of Mechanical and Industrial Engineering, University of Illinois at Chicago, Chicago, IL 60607, USA
[b] Electronic Visualization Laboratory, University of Illinois at Chicago, Chicago, IL 60607, USA

ARTICLE INFO

Keywords:
Deep learning
High entropy alloys
STEM images
Column heights
Elements distribution

ABSTRACT

The latest developments of machine learning (ML) and deep learning (DL) algorithms have paved the way to effectively analyze the atomic structure of chemically-complex materials. In this work, we present a DL model built upon a fully convolutional neural network (FCN) to resolve the random elements distribution of complex PtNiPdCoFe high-entropy alloys (HEAs) represented in the scanning transmission electron microscopy (STEM) images at atomic resolution. The objective of the proposed neural network is to learn through semantic segmentation the non-linear correlations between the pixels' intensities of STEM images and the number of atoms of different constituent elements in the atomic columns (i.e., column heights) in the HEA's structure. We demonstrate that our DL model is capable of correctly estimating the column heights or with an error up to 1 atom for the majority of the columns in the HEA structures represented in the simulated STEM images used to train and test the network. This establishes a sufficiently high level of confidence in the estimation of the element distribution in experimental images. The predicted distributions in different STEM images of nanoparticles reveal inhomogeneous fluctuations with local aggregations in the elemental atomic fractions within the columns. The most pronounced aggregation is displayed by Pt, which is the largest and most electronegative element in the synthesized HEA material. The proposed DL method is beneficial for an in-depth characterization of the structural properties of HEAs and multielement 3D materials in general.

1. Introduction

Chemically-complex alloy nanoparticles (NPs) are of great interest in a wide range of applications including catalysis [1–4], energy storage [5] and bio/plasmonic imaging [6]. Among them, high entropy alloys (HEAs) are an important class of NPs. A pioneering investigation of HEAs was presented by Cantor et al. [7], who considered equiatomic compounds with a number of principal elements up to twenty, including the five-component FeCrMnNiCo alloy (known as the "Cantor alloy" in the literature). One of the most important discoveries of their study was that the equimolar five-element FeCrMnNiCo alloy stabilizes in a single-phase FCC solid solution. The concept of "high entropy" was introduced by Yeh and co-workers [8], who postulated for the first time that multicomponent alloys with five or more elements in nearly equimolar ratio are characterized by a sufficiently high configurational entropy to stabilize randomly mixed solid solution alloys with no intermetallic compounds. However, the formation of non-equiatomic and randomly mixed multicomponent alloys has been demonstrated in more recent studies [9,10]. In general, equiatomic and non-equiatomic HEAs are widely explored compounds because of their exceptional properties compared to conventional alloys [11].

Yeh et al. [12] introduced four major effects characterizing the nature and the versatile properties of HEAs: the high entropy effect, the lattice distortion, the sluggish diffusion and the cocktail effect. Such core features assumed to be related to the randomness of the HEAs compositions, have been extensively described in the literature [13]. The exceptional mechanical [14], thermal [15], electrical [16] and magnetic [17] properties of HEAs have sparked the interest in applications of these materials in many areas of engineering. The understanding of the relationship between the properties and the structural composition of HEAs is crucial for their appropriate design in engineering applications.

The study of the composition of HEAs is tedious mainly because of the combination of different number of elements and different concentrations, resulting in a vast configurational space of potential HEAs.

* Corresponding author.
E-mail address: vyurkiv@uic.edu (V. Yurkiv).

https://doi.org/10.1016/j.commatsci.2021.110905
Received 22 June 2021; Received in revised form 17 September 2021; Accepted 18 September 2021
Available online 30 September 2021

High-throughput computational and experimental methods like Calculation Phase Diagram (CALPHAD) analysis [18], experimental combinatorial techniques [19], and mechanistic-based approach [20] have been proposed to screen HEAs by the identification of co-existing phases together with their compositions and volume fraction. In a more recent publication, Ding and co-workers [21] presented a method based on energy-dispersive X-ray spectroscopy (EDS) to obtain high resolution mapping of the fraction of each chemical element in the atomic columns of HEAs represented in high-angle annular dark field (HAADF) images from transmission electron microscopy (TEM). Despite EDS mapping being a pioneered technique to acquire the atomic-scale mapping of the chemical elements distribution in the atomic columns of synthesized HEAs [22] and solid solutions in general, it does not allow the user to estimate the actual number of atoms distributed in the columns. A more in-depth characterization of the chemical composition of HEAs requires the development of innovative techniques which could allow a precise prediction of the atomic scale distribution.

In a STEM image, the relationship between the pixel intensities and the number of atoms in the atomic columns of a single element NP is assumed to follow a linear relationship, thus the CHs could be extracted via linear interpolation [23]. Van Aert et al. [24] and Backer et al. [25] demonstrated that statistical methods based on parameter estimation theory and least square estimator, respectively, are capable of precisely quantifying the number of atoms arranged in the atomic columns of nanoparticles in HAADF STEM images of different chemical elements. However, the applicability of these methods has been demonstrated only for a single chemical element nanocluster. In general, these methods assume that the intensity of the peaks of the atomic columns in the STEM images is linearly correlated with the corresponding CHs and an increasing intensity is associated with an increasing number of atoms in the atomic columns.

On the other hand, for multicomponent alloys such as HEAs, the pixel intensities of the STEM images are influenced not only by the absolute CHs, but also by the electronic configuration and the distribution of atoms of different chemical elements within the columns. In the STEM process, the pixel intensities depend on the interaction between the incident electron wave and the electronic configuration of the atoms in the structure. Since HEAs are characterized by atoms with varying electronic configurations, each chemical element contributes differently to the pixel intensities in the STEM images. For example, since Pt has the most energetic electronic configuration of $4f^{14}5d^{9}6s^{1}$, columns with a high content of Pt are more likely to display a higher intensity compared to columns rich in Co, which has a lower energetic electronic configuration of $3d^{7}4s^{2}$. In addition, the pixel intensities are also correlated with the position of the atoms in the columns. For instance, atomic columns with the same elemental fractions have different intensities according to the location of the atoms with different electronic configuration in the direction of the incident electron beam. Thus, the random distribution of Pt, Ni, Pd, Co and Fe in the HEAs structure has a strong impact on the intensity values of the atomic columns. In addition, the STEM images acquisition process of multicomponent alloys is characterized by a crosstalk effect [26] for which the pixel intensity of an atomic column depends not only on the composition the column, but also of the neighboring columns around it. Such phenomenon further complicates the estimation of the chemical composition of HEAs using state-of-the-art techniques.

In recent years, ML and DL algorithms have paved the way to a more profound atomic scale understanding of various materials [27–29] and HEAs in particular [30–39]. Kaufmann et al. [30] presented a random forest (RF) model to predict the solid solution forming ability of HEA from thermodynamic and chemical features. Huang and co-workers [31] and Risal et al. [32] have classified HEAs according to the formation of solid solutions (SS), intermetallic (IM) and SS + IM phases using K-nearest neighbors (KNN), support vector machine (SVM) and artificial neural network (ANN). Dai and co-workers [36] predicted the phase formation of HEAs using ML integrated with feature engineering in small datasets. Wen et al. [33] and Kim et al. [34] implanted ML models to predict respectively the hardness and elasticity in different HEAs systems.

DL models built upon convolutional neural networks (CNNs) have been also adopted to successfully predict the thickness of SrTiO3 samples from STEM images [40]. In particular, fully convolutional neural networks (FCNs) have been adopted for a precise estimation of the number of atoms in the atomic columns (i.e., column heights) of Au NPs from high-resolution transmission electron microscopy (HRTEM) images [41,42]. Madsen et al. [41] presented an FCN applied to simulated HRTEM images to classify the atomic columns according to their number of atoms under varying imaging conditions of the microscope parameters. In our prior work, the method was extended to estimate the column heights (CHs) in Au NPs represented in simulated and also experimental HRTEM images, through a regression-based FCN [42] version of the original model developed by Madsen et al. [41]. The DL-based characterization of the 3D shape of metallic NPs proved to be a valid alternative to the state-of-the-art techniques based on electron tomography [43].

In this work, we present a DL approach to predict the number of atoms of different chemical elements in the atomic columns of HEAs represented in simulated and experimental atomic-resolution HAADF STEM images. The method we present here is built upon our prior regression-based FCN work applied to HRTEM images of Au NPs [42], which is extended to the case of multi-element alloys. As a benchmark case, we consider nearly equiatomic PtPdNiCoFe HEA in an FCC single phase solid solution, where inhomogeneous fluctuations with local aggregation of the chemical elements' concentrations in the atomic columns are taken into account. Through semantic segmentation, the proposed FCN is capable of learning the complex and non-linear relationship between the intensities of the atomic column pixels in the HAADF STEM images and the CHs of each different chemical element in the HEA's structure. The neural network is trained and tested on a dataset of simulated HAADF STEM images of HEA NPs and consequently it is applied to predict atomic CHs and element's distribution in experimentally acquired HAADF STEM images of the same type of HEA. The proposed modeling approach allows for a precise estimation of the constituent element's distribution in complex HEAs, being beneficial for the analysis of the structure-properties relationships in these materials. Besides the primary objective of the prediction of the CHs in HEAs structures, this work establishes a basis for an appropriate design of HEAs in engineering applications.

2. Methodology

The modeling framework presented in this work combines density functional theory (DFT) and evolutionary approach (EA) calculations, HEAs, STEM image simulations and DL modeling. First, the DFT and EA calculations are required to develop realistic HEAs atomic models, which are employed to generate the dataset of simulated HAADF STEM images and the necessary ground truth of the atomic CHs for training and testing the neural network. The combined DFT and EA calculations have been performed using the Vienna Ab Initio Simulation Package (VASP) [44] and Atomistic Tool Kit (ATK) [45] as it is described in more detail in Supplementary Information. The simulated HAADF STEM images have been computed for each HEA atomic model, using the multislice algorithm [46], implemented in the PyQSTEM [47] Python library. Within the simulations, the appropriate STEM microscope parameters and resolution have been defined in agreement with the imaging experimental conditions. Finally, the dataset of modeling HAADF STEM images has been used to train and test the DL model. The DL model is an FCN type of neural network and it has been built using the Tensorflow 2.2 [48] library for DL algorithms development. The network has been trained and validated using a cluster of 2 V100 Nvidia GPUs in docker environment built in Kubernetes. The distributed

training with model parallelization technique has been implemented using the Horovod library [49]. The mixed precision and accelerated linear algebra (XLA) [50] technique have been implemented to speed up the computation. A total of approximately 2 months were required to train the model until the desired values of the target metrics have been achieved. Finally, the trained model has been applied to experimental HAADF STEM images to predict the CHs in realistic HEAs. The workflow of the presented modeling framework is illustrated in Fig. 1.

2.1. DFT and EA calculations of HEAs and HAADF STEM images simulations

HEAs are defined as solid solutions with a random distribution of the chemical species, thus the atomic models have been computed by generating NPs with a random size (i.e., diameter) within the range 6.5–7.5 nm of the samples represented in the experimental images, and with a random position of the Pt, Ni, Pd, Co and Fe atoms in the structures. The random HEAs atomic models have been generated on the basis of realistic "atomic motives" identified with DFT and EA methods, as it is described in Supplementary Information. Although in this paper we focus on HEA models with the same size of NPs represented in experimental measurements, our framework is amenable to a variety of sizes according to the application of interest. Fig. 2 illustrates modeled HEAs of different sizes (i.e., diameter) of 2 nm, 4 nm, 6 nm and 8 nm and the corresponding simulated HAADF STEM images. It should be noted that, for bigger sizes only, a portion of the NP can be considered to capture the atomic scale resolution necessary for an appropriate training of the DL model.

We have simulated ideal HEAs with a nearly equiatomic composition, resulting in an element proportion around 20%. In particular, in our modeled HEAs characterized by chemical elements belonging to different rows of transition metals in the Periodic Table (i.e., Ni, Co and Fe belong to the first row, while Pd and Pt belong to the second and third rows, respectively), the internal atomic fraction within the columns exhibits inhomogeneous fluctuations with local aggregations. For example, a chemical element can reach an atomic fraction up to 50% within a column, with a reduction to 2% in a nearby column. In a few columns, a chemical element could even be absent. This type of composition is in agreement with the results obtained by Ding et al. [21] which showed inhomogeneous fluctuations with local aggregations in CrFeCoNiPd HEAs, in contrast to the CrMnFeCoNi Cantor alloys where the atomic fraction of a chemical element in an atomic column randomly fluctuates around 20% with a small variation of approximately 10%. Our HEAs models have been created considering an FCC atomic structure, and the [1 1 0] axis plane as surface orientation in agreement with the experimental HAADF STEM images.

With the aim of training the model with a sufficiently variant dataset of images, we have simulated the HAADF STEM images in local regions

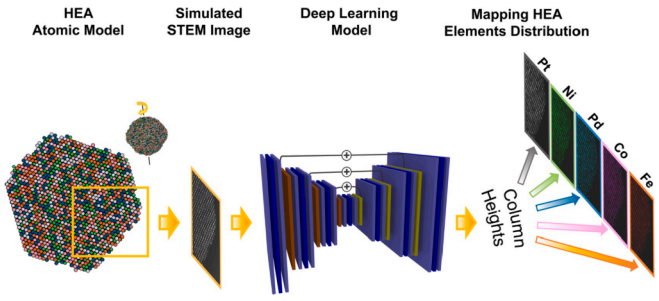

Fig. 1. Illustration of the modeling framework to predict element distribution in HEA materials. Atomic models of PtNiPdCoFe HEAs are computed with DFT and EA to generate the dataset of simulated images for training and testing the DL model. The model is then capable of mapping the element distribution in the HEA structure by predicting the atomic CHs for each chemical element through semantic segmentation.

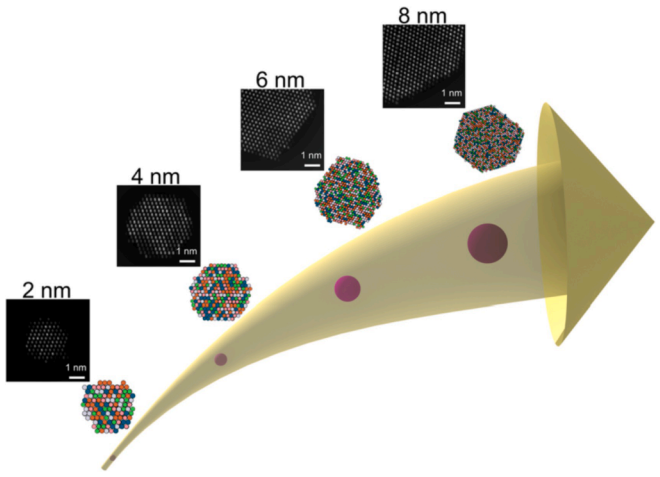

Fig. 2. Atomic models of HEAs with different sizes of the NPs and the corresponding simulated HAADF STEM images. In this work, we have considered a random size within the range 6.5–7.5 nm, but our framework is amenable to any size of interest.

within the structures randomly selected in different locations of the NPs. Such locations could be near the background, in the center of the structures, as well as regions in between. A total of 10,000 random HEA NPs have been generated using the model, resulting in a dataset of 10,000 simulated HAADF STEM images. An example of HEAs atomic model and the corresponding simulated HAADF STEM image and CHs ground truth for each chemical element is illustrated in Fig. 3.

The simulated HAADF STEM images have been computed using the multislice algorithm [46], where a slice thickness of 0.2 nm and a probe size of 8 × 8 nm are considered to simulate images of 6.5–7.5 nm sized HEAs. The STEM microscope parameters, randomly varied in a range centered with respect to the experimental values with a 10% variation, are listed in Table 1. A critical parameter in the STEM images simulation is the appropriate value of the resolution, measured in nm/pixel. The experimental images are characterized by 512 × 512 pixels with 0.01 nm/pixel resolution. In the construction of our training and test datasets, we have considered 256 × 256 images, with an imposed resolution of 0.02 nm/pixel. In this way, the same physical spatial domain of 51.2 × 51.2 nm is preserved. The reason behind the choice of a reduced image size is that 256 × 256 images result in a faster computation as compared to 512 × 512 images. In addition, we have verified that 256 × 256 is the

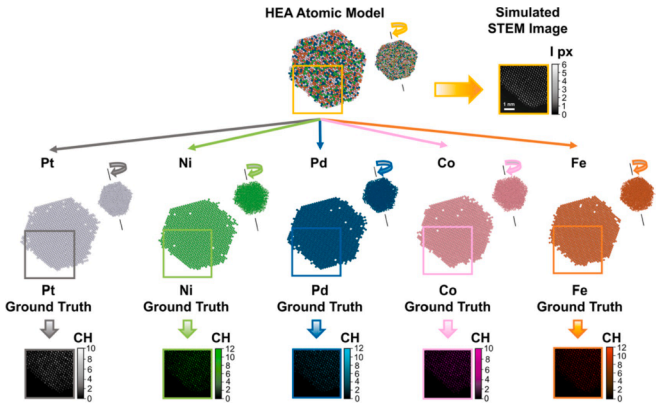

Fig. 3. Example of atomic model of HEA characterized by a nearly equiatomic composition of Pt, Ni, Pd, Co and Fe. The developed HEA atomic model is used to generate the corresponding atomic resolution simulated HAADF STEM image with locally normalized pixel intensity (I px) and the ground truth of the atomic CHs for each chemical element in a random portion of the NP in the [1 1 0] axis plane.

Table 1
STEM microscope parameters used in the HAADF image simulations.

Microscope Parameter	Range
Acceleration voltage / kV	[180, 220]
Convergence angle / mrad	[15, 20]
First order aberration (Cs) / mm	[−5, 5]
Defocus / Å	[−10, 10]
Astigmation magnitude / Å	[18, 22]
Astigmation angle / °	[12, 16]

optimal image size for the DL model, whereas smaller images do not allow the neural network to properly capture the atomic scale resolution. In fact, lower resolution images (i.e., 128 × 128) result in a small, but noticeable, pixilation in the CHs ground truth maps which has a negative impact on the network's performance. On the other hand, higher resolution images (i.e., 512 × 512) require an increased computational time with no significant boost in the model's accuracy.

The implemented simulations reproduce the acquisition of HAADF STEM images of the electron microscope, which provide a 2D representation of the sample with the pixel intensities correlated to the 3D structural configuration. The microscope parameters have been set according to the experimental conditions. These parameters determine the kinematics conditions in the acquisition of the image, and they have a profound effect in resulting pixel intensities of the atomic columns.

In experimental images, a certain degree of noise is typically present. Thus, we have added a random noise to our ideal modeling images, in order to reflect realistic experimental conditions. A combination of subtractive and divisive Gaussian normalization is applied to enhance the intensity of the peaks of the atomic columns with respect to the background between the columns [41]. First, each pixel is subtracted by the minimum intensity value within the original image, and then divided by the difference between the maximum and minimum intensity. Then, a Gaussian filter of the resulting image is subtracted. Finally, each pixel is divided by the squared root of a Gaussian filter of the resulting squared intensity. The inverse of the resolution has been

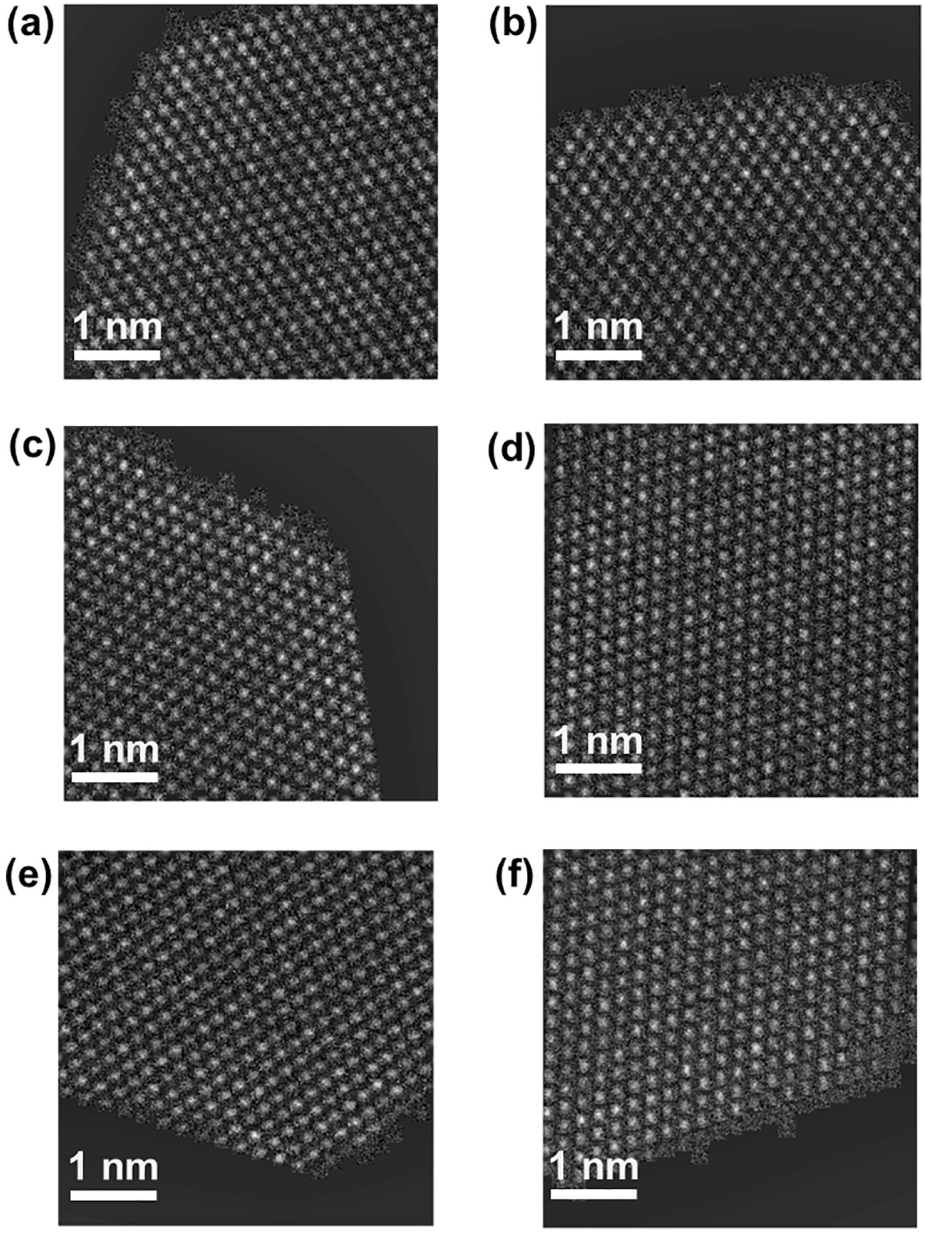

Fig. 4. Examples of simulated HAADF STEM images in random regions of the HEAs structures and random orientations (a–f). The randomness of the locations of the regions and the orientations results in CHs with different values.

chosen as the standard deviation of the Gaussian filter, while the mean has been set to 0. The subtractive and divisive normalization is described in Eqs. (1)–(3):

$$I'_{N\times N} = \frac{I_{N\times N} - \min(I_{N\times N})}{\max(I_{N\times N}) - \min(I_{N\times N})} \quad (1)$$

$$I''_{N\times N} = I'_{N\times N} - G(I'_{N\times N}) \quad (2)$$

$$I'''_{N\times N} = \frac{I''_{N\times N}}{\sqrt{G(I''^{2}_{N\times N})}} \quad (3)$$

$I_{N\times N}$ are the pixel intensities in the $N \times N$ original image (in our case $N = 256$), $I'_{N\times N}$, $I''_{N\times N}$and $I'''_{N\times N}$ are the pixel intensities after the first, second and third steps of the normalization, and the function G is the applied Gaussian filter. The subtractive and divisive normalization results in a range of pixel intensities varying with a Gaussian distribution between a minimum value of 0 for the background and a maximum value at the peak of the atomic columns. Fig. 4 shows six examples of simulated HAADF STEM images depicted in random regions and with random orientations of the modeling HEAs structures in the dataset.

The ground truth of the atomic CHs for each chemical element is likewise constructed with a Gaussian distribution, assigning a value of 0 in correspondence of the background and the actual value of atoms within a column at the pixels corresponding to the peaks. The creation of ground truth maps with pixel values varying continuously from the background to the center of the columns is critical for the implementation of the regression-based semantic segmentation performed by the neural network. The construction of a column height map following a Gaussian distribution motivates the Gaussian filtering applied to the STEM images to enhance the peaks. This approach ensures that the pixel values in the input images have the same type of variation as the pixel values of the ground truth maps. Such a symmetrical correlation is beneficial for the learning process of the neural network.

2.2. Deep learning model

The objective of the supervised DL model is to learn in a supervised fashion the pixel-wise relationship between the intensity of the signal in the HAADF STEM images and the intensity in the segmented features maps, labeled with the values of the CHs for each element in the HEAs structure. The input of the FCN is a HAADF STEM image, while the output is a series of features maps representing the corresponding CHs for each chemical element, with the same spatial dimensionality of the input. The network's architecture is the same as that adopted in our prior publication [42], except for the last inference layer, comprising of a number of output channels corresponding to the number of chemical elements (i.e., five in this case). The model is an encoder-decoder type of neural network, characterized by a series of three blocks of convolutional layers in the encoder side (i.e., convolution) and a symmetrical series of three blocks of convolutional layers in the decoder side (i.e., deconvolution). Between the encoder and the decoder, a "bridge" of convolutional layers is present. Each convolutional layer is characterized by 3×3 filters to extract the feature values of the input image (i.e., pixel values) and a rectified linear unit (ReLU) activation function. Batch normalization is also used to increase the stability of the network. In order to avoid the problem of the vanishing gradient during the learning process, the convolutional blocks are built with two convolutional layers and a residual block of three convolutional layers in between, and skipped connections are used to connect a block in the encoder with its symmetrical counterpart in the decoder. The encoder is responsible for the down-sampling of the input image using max-pooling layers after each convolutional block, while the decoder sequentially restores the original size of the input incorporating up-sampling layers at the end of each convolutional block. In our case, we have considered 256×256 images but the network is amenable to arbitrary sizes. The first, second and third convolutional blocks of the encoder and their symmetrical counterpart in the decoder have 32, 64 and 128 channels respectively. The convolutional layers in the bridge block have 256 channels. The last layer of the network is a convolutional layer with a 1×1 filter and five output channels, which predict the segmented features maps representing the atomic CHs of the five chemical elements. The network is trained using the Adam optimizer, the mean squared error (MSE) as loss function and a batch size of 32 images.

3. Results and discussion

In this section, we first describe a statistical study of the correlations between the pixel intensities in the simulated STEM images and the CHs of the represented HEA sample. Then, we illustrate the CHs prediction in the simulated images and the corresponding performance analysis. Finally, we present the estimation of the CHs in HEAs in STEM images acquired in experimental measurements as a demonstration of the applicability of our modeling framework to realistic cases.

3.1. Statistical analysis of the pixel intensities-column heights correlation in HAADF STEM images of HEAs

Herein, the correlation between the pixel intensities in the simulated HAADF STEM images and the CHs for each chemical element is described. In particular, we consider the signal in the center of the columns, referred to as "peaks." Both the STEM images and the CHs label maps are created using a Gaussian filtering technique. For this reason, the columns' peaks in the STEM images correspond to the brightest pixel values, and likewise, they correspond to the actual number of atoms in the columns in the CHs label maps. The scope of this study is to investigate how the composition of elements in CHs influence the intensity of the pixels in the STEM image.

The correlation between the STEM pixel values and the CHs is considered for each chemical element separately. In particular, we demonstrate that such relationship is highly nonlinear and each chemical element has a different correlation with respect to the others. The correlation is analyzed considering the scatter plot of the columns' peaks intensity as a function of the CHs for each chemical element. In addition, a linear fit is performed to investigate how the correlations deviate from a typical linear STEM behavior. The slope of the linear fitting explains the tendency of an enhanced intensity by increasing the number of atoms in the columns, while the R-Square reveals the closeness to a linear trend. Fig. 5 illustrates the results for an HEA randomly selected from the dataset.

Fig. 5 illustrates that each element has a different correlation of the peak's intensities with respect to the CHs. In particular, the linear fit reveals that Pt is the element characterized by the highest slope and highest R-Square of 0.366 and 0.308, followed by Pd with a slope of 0.134 and R-Square of 0.035. Such behavior could be due to the most energetic electronic configurations of $4f^{14}5d^{9}6s^{1}$ and $4d^{10}$of Pt and Pd respectively. On the other hand, Ni, Co and Fe have the lowest slope of 0.029, 0.057, and 0.072 and R-Square of 0.002, 0.007 and 0.011, since the electronic configurations of $3d^{8}4s^{2}$, $3d^{7}4s^{2}$ and $3d^{6}4s^{2}$ respectively are less energetic. It could be noted that in this particular HEA, Ni has slightly lower slope and R-square compared to Co and Fe, despite it has one and two additional atoms in the outer shell. Such result could be due to the random distribution of the atoms in the columns, which together with the electronic configuration has an impact on the pixel intensities in the STEM images. The peaks pixel values range from -1 up to 10 as a result of the applied Gaussian filtering.

Furthermore, Fig. 5 shows that for a single chemical element, columns with the same heights have different intensity and indeed, some columns with a lower number of atoms are characterized by a stronger signal compared to higher columns and vice-versa. This behavior is due to the random distribution of the chemical elements in the columns. For

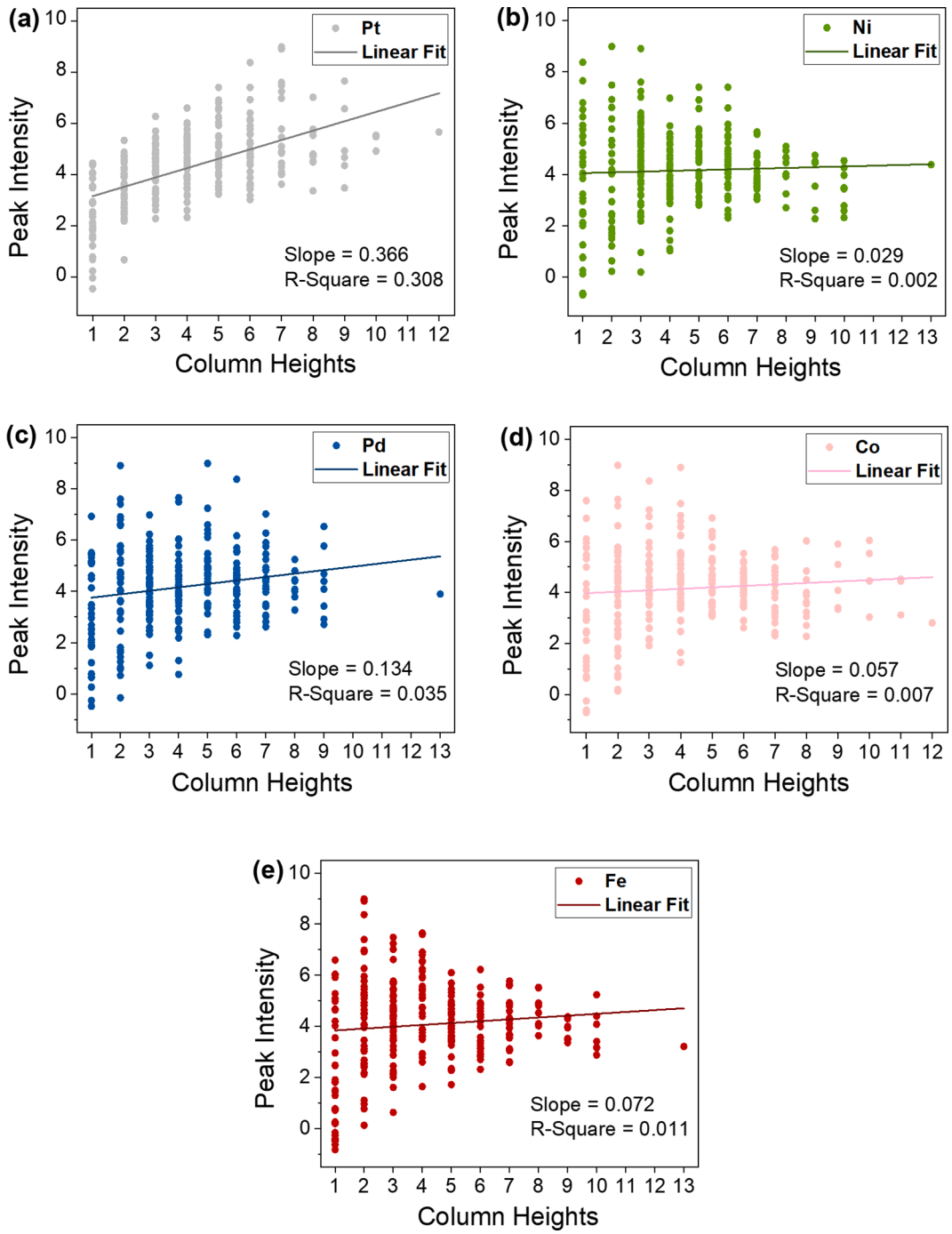

Fig. 5. Scatter plots and corresponding linear fitting representing the relationship between the pixel intensities of a simulated STEM in the peaks of the atomic columns and the corresponding CHs for Pt (a), Ni (b), Pd (c), Co (d), and Fe (e) for an HEA randomly selected from the dataset.

example, atoms impact the intensity differently depending on their location, which could be in the top or in the bottom of the column. In particular, a high CH of a certain element could have a lower intensity compared to a shorter CH, if the column is rich of other atoms with a low energetic electronic configuration placed on top of the column. The non-linear correlation between pixel intensities and CHs is also contributed by the crosstalk effect [26] present in the STEM images, though the systematic study of such effect is beyond the scope of this work.

In summary, the relationship between the peak's intensity and the CHs for each chemical element in STEM images of HEAs is highly non-linear due to the combination of the electronic configuration, element distribution and crosstalk effect. For this reason, more advanced techniques compared to the state-of-the-art methods are required to predict the atomic scale distribution of HEAs from STEM images. In this work, we demonstrate that DL modeling based on FCN's semantic segmentation of HAADF STEM images has the potential to capture such non-linear correlations and closely estimate the CHs in HEAs.

3.2. Training and test results of the DL model applied to the modeling HAADF STEM images

The DL model requires to be appropriately trained to recognize the CHs for each element in HEAs structures represented in the STEM images. The learning process of the neural network is implemented

through an iterative process of successive steps called epochs, characterized by updates of the model's parameters (i.e., weights and bias) towards an optimal performance. At each epoch, the FCN processes different simulated HAADF STEM images and the corresponding ground truth and it learns the relationship between the pixel's intensities and the CHs in a supervised fashion. In order to enhance the variance of the model, which is beneficial for the learning process of statistical learning algorithms, a variety of random transformations including contrast, illumination, blur and rotations are applied to the input images at each epoch. It should be noted that a significant contribution to the variance of the dataset is provided also by the randomness of the HEAs structures and the considered random portions, as well as to the values of microscope's parameters randomly varied in a range centered with respect to the imaging experimental conditions.

The performance of the model is monitored through the mean squared error (MSE) loss, which is minimized towards a global minimum at each epoch. In addition to the MSE loss, the efficacy of the neural network is verified considering the typical regression metric R^2, computed between the predicted and the true CHs for each chemical element. Compared to the MSE loss which performs a standard pixel-wise comparison between the model's inference and the ground truth, we have calculated the R^2 only for the pixels corresponding to the peaks, thus it provides a more physical interpretation to the performance of the FCN. The optimal value of the R^2 is 1, corresponding to a perfect agreement between the predicted and the true CHs.

The training and the test process have been performed simultaneously at each epoch in order to implement an online control of the underfitting (i.e., non-accurate training and test performance) and overfitting (accurate training and non-accurate test performance) issues which could affect statistical learning models. We have verified that a dataset of 10,000 images is appropriate to train and test the neural network to prevent both underfitting and overfitting in our model. For this purpose, the training dataset has been built considering 8,000 images randomly selected from the dataset, while the remaining 2,000 images have been used to test the model.

The training and test learning curves (i.e., the profiles of values of the metrics for each epoch) of the MSE loss, the R^2 for Pt, Ni, Pd, Co and Fe as well as the average R^2 among the five elements are illustrated in Fig. S3 of Supplementary Information. The learning curves of the R^2 metric for each element reveals that Pt and Pd are the fastest elements in improving their performance, and that a delay over the epochs is observed for Ni and Fe and most significantly for Co. The physical interpretation of the delay of the model's performance among the five chemical elements could be provided by examining the values of the slope and R-Square describing the correlations between the pixel's intensities in the HAADF STEM images and the CHs for Pt, Ni, Pd, Co and Fe reported in Fig. 5. Since Pt is characterized by the highest values of the slope and R-Square, it is the element most likely to be close to a typical linear behavior in STEM images representing NPs of a single chemical element, for which the intensity linearly increases with the CHs. On the contrary, the analysis has demonstrated that Ni, Fe and in particular Co have a highly nonlinear behavior. Thus, it is more straightforward for the neural network to capture the correlation between the pixel's intensities and the CHs for Pt and Pd, while a major effort is required to learn the highly nonlinear profile of Ni, Fe and Co. The resulting behavior of the learning process is a remarkable observation which describes how the DL model is instructed by the physics of the HEAs structures in our dataset. In particular, this work demonstrates how the features of the HEAs related to the electronic configurations and the random distributions of the elements are the driving force guiding the optimization process implemented in our statistical learning algorithm.

The FCN is trained for 800 epochs in order to achieve a satisfactory R^2 above 0.70 for each element. Fig. 6 illustrates a prediction of the CHs for each element in a STEM image randomly selected from the test

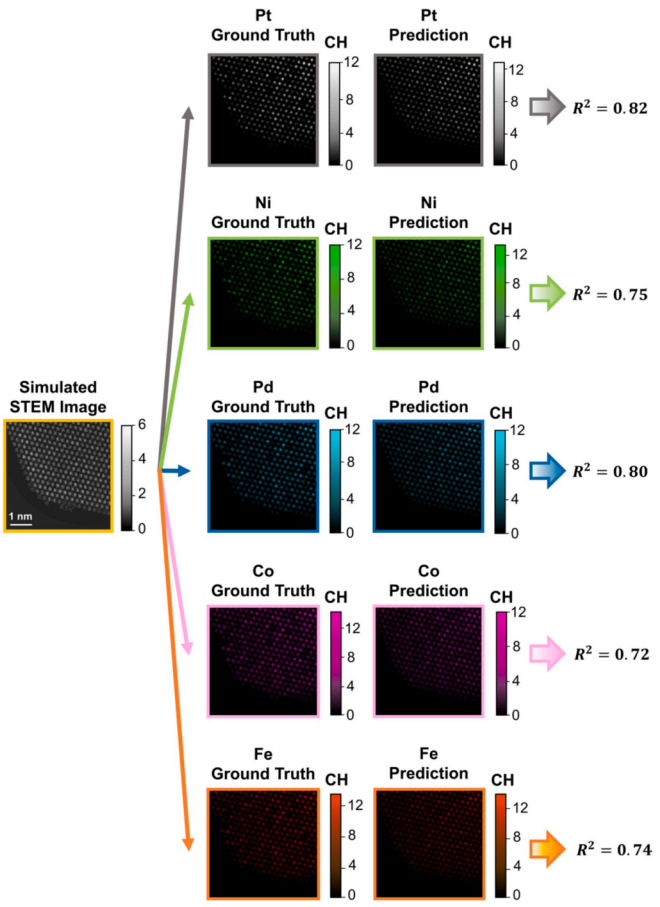

Fig. 6. Prediction of the atomic CHs for each chemical element performed by the DL model applied to a simulated HAADF STEM randomly selected from the dataset. Pt and Pd exhibit the highest values of the R^2 calculated between the predicted and the true eights.

dataset. The figure shows that a more precise prediction of the CHs is obtained for Pt and Pd with a value of R^2 equal to 0.82 and 0.80 respectively, while Ni, Co and Fe exhibit slightly lower performances. Although the R^2 values between the predicted and the true CHs provide quantitative characterization of the regression task performed by the model, a detailed analysis of the errors in the estimated number of atoms for different CHs allows a broader qualitative assessment of the network's performance. Figs. S4–S8 in Supplementary Information show an error distribution highlighting the differences between the true and the predicted values for each CHs and for each element. In particular, we demonstrate that for each element, the majority of the columns are predicted with a difference of just 1 atom with respect to the ground truth. For example, in the Pt prediction ($R^2 = 0.82$) illustrated in Fig. 6, 50% of the columns are predicted with the correct CHs, whereas an error of 1, 2, and 3 atoms is reported for the 41%, 7%, and 2% of the columns. Errors of 4 or more atoms are not reported. In particular, an error of 1 atom is equally distributed in columns with different CHs, while errors of 2 and 3 tend to be concentrated in higher CHs such as 8, 9 and 10. Comparing the error distribution for different elements, Pd, Ni, Co and Fe shows higher fractions of mistaken columns, but in all cases the maximum error is 3 atoms, which is reported for less than 5% of the columns. Thus, a confidence band of $\pm$ 1 atom is reported for 91% of the columns in the optimal case of Pt (50% correct + 41% with an error of 1 atom) and around 77% or higher for the other elements, while a confidence band of $\pm$ 2 atoms is reported for more than 95% of the columns for all the elements. Such level of accuracy is comparable to the method reported by LeBeau et al. [23], where 86% and 99% of the columns have confidence bands of $\pm$1 and 2 atoms respectively. However, the novelty

introduced by our proposed method is the application to complicated quinary HEAs compared to the single element nanoparticles reported in the literature. The analysis is reported here for a random image, but similar results are obtained for the other HEAs in the training and test datasets. In general, we have verified that the majority of the columns are predicted correctly or with an error of only 1 atom. The statistics of the CHs errors for the prediction in Fig. 6 are provided in Table 2.

In conclusion, our DL model is capable of predicting precisely the CHs in HEAs represented in simulated HAADF STEM images. Since the model has been trained and tested on images and HEAs models representing realistic conditions, the same performance could be expected in the application of the model to the experimental images.

3.3. Prediction of the column heights distribution in experimental HAADF STEM images

Here we show the application of our trained DL model to experimental HAADF STEM images of HEAs represented in different regions of the alloys. Fig. 7 illustrates a portion of an HEA close to the background, while in Fig. 8 a central region of another alloy is considered. In addition to the CH maps predicted by the FCN, statistical distributions of the predicted CHs and the atomic fraction within the columns for each chemical element are analyzed.

Fig. 7a shows that the FCN predicts an approximately even distribution of Pt, Ni, Pd, Co and Fe, since the CHs vary in a similar range. However, a slightly higher content of atoms is reported for Pt and Fe. It can be noted that the composition is nearly equiatomic, with a 23% and 25% for Pt and Fe, and 17%, 18%, 17% for Ni, Pd and Co. These values are physically reasonable for this type of alloy. In addition, Fig. 7b provides the distribution of the CHs for the five elements. For each element, the reported profiles are close to each other, as a result of the nearly equiatomic composition, while CHs 4 and 5 are the most populated given the size of the alloy. Such distribution follows the same profile of the CHs distribution in the simulated images illustrated in Fig. S2 in Supplementary Information. However, it could be noted that for CHs higher than 7, Pt and Fe count more columns compared to Ni, Pd and Co, explaining the higher concentrations for these two elements. Furthermore, Fig. 7c shows the variation of the atomic fractions within the columns, which is typically evaluated through EDS mapping and pair correlations analysis in experimental measurements [51]. We have verified that inhomogeneous fluctuations with local aggregations are present in the HEA under consideration. For instance, some atomic fractions of Pt and Fe are higher than 50% in some columns. Likewise, some atomic fractions could be below 10%. However, the local clustering is present only at the column level, while ordinate clusters of columns rich of a single element do not form. The profile in Fig. 7c is in agreement with the results obtained by Ding et al. [21], who illustrated that inhomogeneous fluctuations with local aggregations could exist in a nearly equiatomic CrFeCoNiPd HEA, characterized by elements with different electronegativity. The local clustering suggests that short-range order may be present in HEAs, meaning that the structural composition is not completely random as postulated in the original definitions for a Cantor alloy characterized by constituent elements with

Table 2
Statistics of the errors in the prediction of the DL model for Pt, Ni, Pd, Co and Fe.

	Pt columns/ %	Ni columns/ %	Pd columns/ %	Co columns/ %	Fe columns/ %
Correct	50 %	33%	35%	34%	35%
Error = 1 atom	41%	44%	49%	43%	42%
Error = 2 atoms	7%	19%	14%	19%	19%
Error = 3 atoms	2%	4%	2%	4%	4%

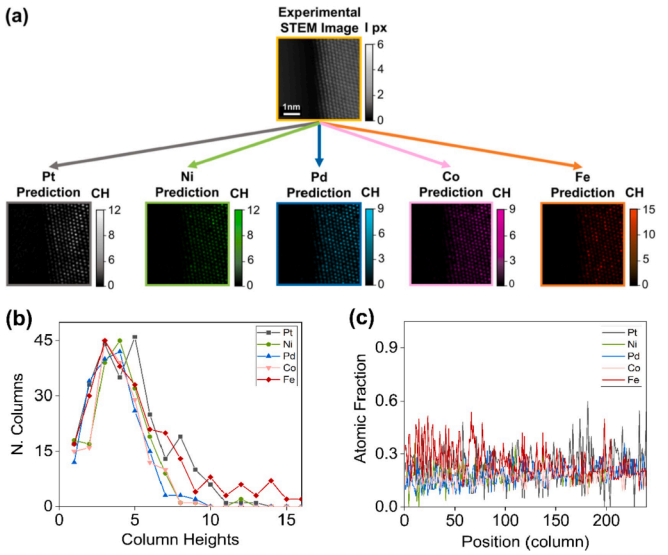

Fig. 7. Prediction of the DL model applied to an experimental HAADF STEM image of a PtNiPdCoFe HEA in a region close to the background. CH maps predicted by the model (a). Predicted CHs distribution (b). Predicted atomic fraction of the five elements within the columns (c).

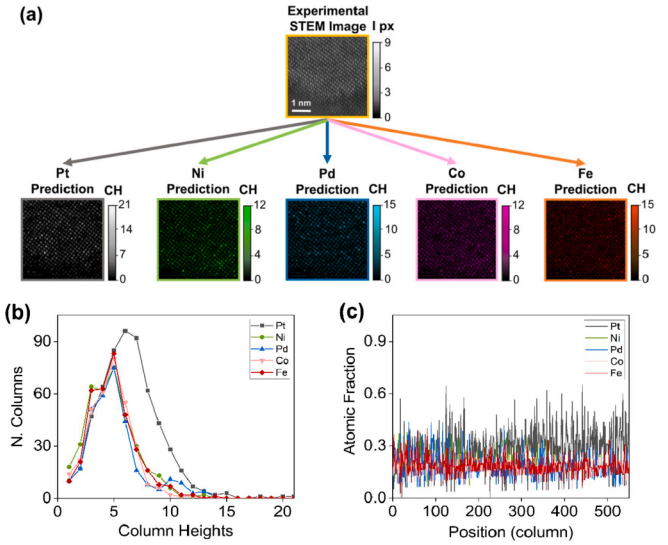

Fig. 8. Prediction of the DL model applied to an experimental HAADF STEM image of a PtNiPdCoFe HEA in a central region of the alloy. CH maps predicted by the model (a). Predicted CHs distribution (b). Predicted atomic fraction of the five elements within the columns (c).

similar size and electronegativity.

In addition, we have considered a central region of another HEA. Fig. 8a reveals that Pt is characterized by the highest range of variation, with a maximum CH of 21, while Ni, Pd, Co and Fe vary in approximately the same range up to 12 and 15 atoms. Indeed, Pt has a concentration of 27%, whereas Ni, Pd, Co and Fe have an approximately equal concentration around 18%. The dominance of Pt in this structure is physically acceptable, as an element concentration could vary up to 35%, according to the original definition provided by Yeh et al. [8]. Fig. 8b shows that also in this case CHs 4 and 5 are the most populated for each element and that Pd exhibits a major number of columns with CHs between 5 and 10 compared to other elements. However, the Pt CH map predicted by the model does not show a presence of a cluster of high columns, whereas an even distribution of the element's concentration is still present despite the abundancy of Pt. The lack of incipient

segregation is also demonstrated by Fig. 8c, which shows that although Pt could achieve an atomic fraction up to 60% in a column, such concentration drops in nearby columns.

Comparing the predicted profile of the atomic fractions in Fig. 7c and c, it could be noted that in both cases Pt is the element characterized by the most pronounced aggregation at column level, with the highest atomic fraction approximately around 60%. Such clustering could be induced by the larger size and higher electronegativity of Pt compared to the other elements, as it is suggested for the first time by Ding and coworkers [21]. In their CrFeCoNiPd HEAs, Pd was larger and most electronegative element, and the EDS analysis exhibited a larger variation up to 58%. Our DL predictions confirm these breakthrough discoveries, revealing that inhomogeneous distribution could be present in HEAs. The inhomogeneous element distribution has fundamental importance, since it results in non-uniform distribution of lattice strain, affecting the microscopic deformation mechanisms in HEAs. Such elemental composition has a profound influence on the mechanical properties of HEA, in particular the stress-strain relationship and the material hardening which are of high interest in practical engineering applications. In experimental measurements, it is not possible to experimentally measure the number of atoms of different chemical elements in the atomic columns. Nevertheless, EDS and EELS spectra could be used to acquire a high resolution mapping of the fractional composition of different chemical elements in complex atomic structures, including high entropy alloys (HEAs) [21]. Future work will be focused on the acquisition of EDS and EELS mapping of HEAs, with the aim of validating the network's prediction of the experimental images.

4. Summary and conclusions

HEAs are characterized by many unique properties comparing to conventional binary alloys, and they are of high interest for applications in catalysis, energy storage and bio/plasmonic imaging. The knowledge of the atomic scale distribution of HEAs is important for a more comprehensive characterization of these materials at the fundamental level. In this work, we describe and demonstrate a deep learning framework for the estimation of the element distribution in the atomic columns of HEAs, through semantic segmentation of HAADF STEM images.

For this purpose, the multislice algorithm and Gaussian filtering are used to generate a dataset of simulated STEM images representing nearly equiatomic PtNiPdCoFe HEAs, with structural characteristics in agreement with the samples observed in the experimental measurements. Performing a statistical analysis of the simulated STEM images, we have demonstrated that the correlation between the pixel intensities and the CHs of the constituent elements is highly nonlinear, because of the random distribution, the different electronegativity of the constituent elements and the crosstalk effect. For this reason, DL modeling represents an advancement towards the characterization of the 3D configuration of HEAs, compared to the state-of-the-art techniques based on electron tomography and statistical parameter estimation theory.

We illustrate that in the simulated HAADF STEM images, our FCN predicts the CHs with a maximum error of three atoms, although the majority of the columns are predicted correctly and with an error of just one atom. The trained network is then applied to two experimental HAADF STEM images. The first image represents an HEA in a region close to the background, whereas the second image illustrate a different HEA in a central region. In the first case, the FCN predicts a slightly higher concentration for Pt and Fe at 23% and 25%, but an overall even distribution of the five constituent elements (i.e., no local clusters of single element rich columns), with inhomogeneous fluctuations with local aggregations at a column level. On the other hand, the prediction for the second image reveals a higher Pt concentration around 27%, while the other elements are nearly equally distributed with a concentration of approximately 18%. As in the first image, the elements are evenly distributed, and the atomic fraction within the columns exhibits inhomogeneous fluctuations with local aggregations. In both cases, Pt is the element which achieves the highest atomic fraction within a column around 60%, confirming a theory developed on the basis of previous experimental studies using EDS mapping of HAADF images of CrFeCoNiPd HEAs, for which the larger and more electronegative element gives rise to a local aggregation in a column's distribution.

The mapping of the HEAs element distribution via DL presented in this work allows for a more accurate characterization and engineering of the mechanical properties of HEAs. Based on the results presented in this report, future work could be focused on estimation of the stress-strain relationship and elastic-plastic deformation in the HEAs predicted by the DL model. Although our method is applied to HEAs with five chemical elements, it is amenable to other HEAs characterized by different number of elements and compositions. Furthermore, the modeling framework proposed in this report represents a general attempt for the identification of chemical species in 3D materials, which is applicable to many atomic configurations other than HEAs. Thus, in addition to the estimation of the number of atoms in the atomic columns of HEAs, our work represents an advancement to the development of computer vision techniques based on statistical learning methods for microscopy analysis, which could be beneficial to a broad area of nanoscience applications.

CRediT authorship contribution statement

Marco Ragone: Conceptualization, Investigation, Code development, Writing and editing. **Mahmoud Tamadoni Saray:** Investigation, Editing. **Lance Long:** Software, Editing. **Reza Shahbazian-Yassar:** Conceptualization, Editing and Project administration. **Farzad Mashayek:** Conceptualization, Editing and Project administration. **Vitaliy Yurkiv:** Conceptualization, Investigation, Code development, Writing, Editing and Project administration.

Declaration of Competing Interest

The authors declare that they have no known competing financial interests or personal relationships that could have appeared to influence the work reported in this paper.

Acknowledgement

The authors acknowledge the financial support from the National Science Foundation, award DMR-2055442, as well as CNS-1828265.

Appendix A. Supplementary data

Supplementary data to this article can be found online at https://doi.org/10.1016/j.commatsci.2021.110905.

References

[1] P.-C. Chen, X. Liu, J.L. Hedrick, Z. Xie, S. Wang, Q.-Y. Lin, M.C. Hersam, V. P. Dravid, C.A. Mirkin, Polyelemental nanoparticle libraries. For target atoms, Science 352 (2016) 1565, https://doi.org/10.1126/science.aaf8402.
[2] L. Bu, N. Zhang, S. Guo, X.u. Zhang, J. Li, J. Yao, T. Wu, G. Lu, J.-Y. Ma, D. Su, X. Huang, Biaxially strained PtPb/Pt core/shell nanoplate boosts oxygen reduction catalysis, Science 354 (6318) (2016) 1410–1414, https://doi.org/10.1126/science:aah6133.
[3] S.G. Kwon, G. Krylova, P.J. Phillips, R.F. Klie, S. Chattopadhyay, T. Shibata, E. E. Bunel, Y. Liu, V.B. Prakapenka, B. Lee, E.V. Shevchenko, Heterogeneous nucleation and shape transformation of multicomponent metallic nanostructures, Nat. Mater. 14 (2015) 215–223, https://doi.org/10.1038/nmat4115.
[4] M. Takahashi, H. Koizumi, W.J. Chun, M. Kori, T. Imaoka, K. Yamamoto, Finely controlled multimetallic nanocluster catalysts for solvent-free aerobic oxidation of hydrocarbons, Sci. Adv. 3 (2017) 1–9, https://doi.org/10.1126/sciadv.1700101.
[5] N.A. Frey, S. Peng, K. Cheng, S. Sun, Magnetic nanoparticles: Synthesis, functionalization, and applications in bioimaging and magnetic energy storage, Chem. Soc. Rev. 38 (2009) 2532–2542, https://doi.org/10.1039/b815548h.

[6] M.B. Cortie, A.M. McDonagh, Synthesis and optical properties of hybrid and alloy plasmonic nanoparticles, Chem. Rev. 111 (6) (2011) 3713–3735, https://doi.org/10.1021/cr1002529.

[7] B. Cantor, I.T.H. Chang, P. Knight, A.J.B. Vincent, Microstructural development in equiatomic multicomponent alloys, Mater. Sci. Eng. A 375–377 (2004) 213–218, https://doi.org/10.1016/j.msea.2003.10.257.

[8] J.W. Yeh, S.K. Chen, S.J. Lin, J.Y. Gan, T.S. Chin, T.T. Shun, C.H. Tsau, S.Y. Chang, Nanostructured high-entropy alloys with multiple principal elements: Novel alloy design concepts and outcomes, Adv. Eng. Mater. 6 (2004) 299–303, https://doi.org/10.1002/adem.200300567.

[9] M.J. Yao, K.G. Pradeep, C.C. Tasan, D. Raabe, A novel, single phase, non-equiatomic FeMnNiCoCr high-entropy alloy with exceptional phase stability and tensile ductility, Scr. Mater. 72–73 (2014) 5–8, https://doi.org/10.1016/j.scriptamat.2013.09.030.

[10] C.G. Schön, T. Duong, Y. Wang, R. Arróyave, Probing the entropy hypothesis in highly concentrated alloys, Acta Mater. 148 (2018) 263–279, https://doi.org/10.1016/j.actamat.2018.01.028.

[11] D.B. Miracle, O.N. Senkov, A critical review of high entropy alloys and related concepts, Acta Mater. 122 (2017) 448–511, https://doi.org/10.1016/j.actamat.2016.08.081.

[12] J.-W. Yeh, Recent progress in high-entropy alloys, Ann. Chim. Sci. Des Mater. 31 (6) (2006) 633–648, https://doi.org/10.3166/acsm.31.633-648.

[13] Y. Zhang, T.T. Zuo, Z. Tang, M.C. Gao, K.A. Dahmen, P.K. Liaw, Z.P. Lu, Microstructures and properties of high-entropy alloys, Prog. Mater. Sci. 61 (2014) 1–93, https://doi.org/10.1016/j.pmatsci.2013.10.001.

[14] A. Gali, E.P. George, Tensile properties of high- and medium-entropy alloys, Intermetallics 39 (2013) 74–78, https://doi.org/10.1016/j.intermet.2013.03.018.

[15] H.-P. Chou, Y.-S. Chang, S.-K. Chen, J.-W. Yeh, Microstructure, thermophysical and electrical properties in AlxCoCrFeNi ($0 \leq x \leq 2$) high-entropy alloys, Mater. Sci. Eng. B Solid-State Mater. Adv. Technol. 163 (3) (2009) 184–189, https://doi.org/10.1016/j.mseb.2009.05.024.

[16] Y.-F. Kao, S.-K. Chen, T.-J. Chen, P.-C. Chu, J.-W. Yeh, S.-J. Lin, Electrical, magnetic, and Hall properties of AlxCoCrFeNi high-entropy alloys, J. Alloys Compd. 509 (5) (2011) 1607–1614, https://doi.org/10.1016/j.jallcom.2010.10.210.

[17] Y. Zhang, T. Zuo, Y. Cheng, P.K. Liaw, High-entropy alloys with high saturation magnetization, electrical resistivity, and malleability, Sci. Rep. 3 (2013) 1–7, https://doi.org/10.1038/srep01455.

[18] F. Zhang, C. Zhang, S.L. Chen, J. Zhu, W.S. Cao, U.R. Kattner, An understanding of high entropy alloys from phase diagram calculations, Calphad Comput. Coupling Phase Diagrams Thermochem. 45 (2014) 1–10, https://doi.org/10.1016/j.calphad.2013.10.006.

[19] Z. Li, A. Ludwig, A. Savan, H. Springer, D. Raabe, Combinatorial metallurgical synthesis and processing of high-entropy alloys, J. Mater. Res. 33 (19) (2018) 3156–3169, https://doi.org/10.1557/jmr.2018.214.

[20] Z. Li, D. Raabe, Strong and Ductile Non-equiatomic High-Entropy Alloys: Design Processing, Microstructure, and Mechanical Properties, Jom 69 (2017) 2099–2106, https://doi.org/10.1007/s11837-017-2540-2.

[21] Q. Ding, Y. Zhang, X. Chen, X. Fu, D. Chen, S. Chen, L. Gu, F. Wei, H. Bei, Y. Gao, M. Wen, J. Li, Z.e. Zhang, T. Zhu, R.O. Ritchie, Q. Yu, Tuning element distribution, structure and properties by composition in high-entropy alloys, Nature 574 (7777) (2019) 223–227, https://doi.org/10.1038/s41586-019-1617-1.

[22] Y. Yao, Z. Huang, P. Xie, S.D. Lacey, R.J. Jacob, H. Xie, F. Chen, A. Nie, T. Pu, M. Rehwoldt, D. Yu, M.R. Zachariah, C. Wang, R. Shahbazian-Yassar, J. Li, L. Hu, Carbothermal shock synthesis of high-entropy-alloy nanoparticles, Science (80-.) 359 (2018) 1489–1494. 10.1126/science.aan5412.

[23] J.M. LeBeau, S.D. Findlay, L.J. Allen, S. Stemmer, Standardless atom counting in scanning transmission electron microscopy, Nano Lett. 10 (11) (2010) 4405–4408, https://doi.org/10.1021/nl102025s.

[24] S. Van Aert, A. De Backer, G.T. Martinez, B. Goris, S. Bals, G. Van Tendeloo, A. Rosenauer, Procedure to count atoms with trustworthy single-atom sensitivity, Phys. Rev. B 87 (2013) 1–6, https://doi.org/10.1103/PhysRevB.87.064107.

[25] A. De Backer, K.H.W. van den Bos, W. Van den Broek, J. Sijbers, S. Van Aert, StatSTEM: An efficient approach for accurate and precise model-based quantification of atomic resolution electron microscopy images, Ultramicroscopy 171 (2016) 104–116, https://doi.org/10.1016/j.ultramic.2016.08.018.

[26] N. Baladés, M. Herrera, D.L. Sales, M.P. Guerrero, E. Guerrero, P.L. Galindo, S. I. Molina, Influence of the crosstalk on the intensity of HAADF-STEM images of quaternary semiconductor materials, J. Microsc. 273 (1) (2019) 81–88, https://doi.org/10.1111/jmi.12763.

[27] Q. Luo, E.A. Holm, C. Wang, A transfer learning approach for improved classification of carbon nanomaterials from TEM images, Nanoscale Adv. (2020), https://doi.org/10.1039/d0na00634c.

[28] N.C. Frey, D. Akinwande, D. Jariwala, V.B. Shenoy, Machine learning-enabled design of point defects in 2d materials for quantum and neuromorphic information processing, ACS Nano 14 (10) (2020) 13406–13417, https://doi.org/10.1021/acsnano.0c05267.

[29] O. Voznyy, L. Levina, J.Z. Fan, M. Askerka, A. Jain, M.-J. Choi, O. Ouellette, P. Todorović, L.K. Sagar, E.H. Sargent, Machine Learning Accelerates Discovery of Optimal Colloidal Quantum Dot Synthesis, ACS Nano 13 (10) (2019) 11122–11128, https://doi.org/10.1021/acsnano.9b03864.

[30] K. Kaufmann, K.S. Vecchio, Searching for high entropy alloys: A machine learning approach, Acta Mater. 198 (2020) 178–222, https://doi.org/10.1016/j.actamat.2020.07.065.

[31] W. Huang, P. Martin, H.L. Zhuang, Machine-learning phase prediction of high-entropy alloys, Acta Mater. 169 (2019) 225–236, https://doi.org/10.1016/j.actamat.2019.03.012.

[32] S. Risal, W. Zhu, P. Guillen, L. Sun, Improving phase prediction accuracy for high entropy alloys with Machine learning, Comput. Mater. Sci. 192 (2021), 110389, https://doi.org/10.1016/j.commatsci.2021.110389.

[33] C. Wen, Y. Zhang, C. Wang, D. Xue, Y. Bai, S. Antonov, L. Dai, T. Lookman, Y. Su, Machine learning assisted design of high entropy alloys with desired property, Acta Mater. 170 (2019) 109–117, https://doi.org/10.1016/j.actamat.2019.03.010.

[34] G. Kim, H. Diao, C. Lee, A.T. Samaei, T. Phan, M. de Jong, K. An, D. Ma, P.K. Liaw, W. Chen, First-principles and machine learning predictions of elasticity in severely lattice-distorted high-entropy alloys with experimental validation, Acta Mater. 181 (2019) 124–138, https://doi.org/10.1016/j.actamat.2019.09.026.

[35] R. Machaka, Machine learning-based prediction of phases in high-entropy alloys, Comput. Mater. Sci. 188 (2021), 110244, https://doi.org/10.1016/j.commatsci.2020.110244.

[36] D. Dai, T. Xu, X. Wei, G. Ding, Y. Xu, J. Zhang, H. Zhang, Using machine learning and feature engineering to characterize limited material datasets of high-entropy alloys, Comput. Mater. Sci. 175 (2020), 109618, https://doi.org/10.1016/j.commatsci.2020.109618.

[37] S.Y. Lee, S. Byeon, H.S. Kim, H. Jin, S. Lee, Deep learning-based phase prediction of high-entropy alloys: Optimization, generation, and explanation, Mater. Des. 197 (2021), 109260, https://doi.org/10.1016/j.matdes.2020.109260.

[38] Z. Zhou, Y. Zhou, Q. He, Z. Ding, F. Li, Y. Yang, Machine learning guided appraisal and exploration of phase design for high entropy alloys, NPJ Comput. Mater. 5 (2019) 1–9, https://doi.org/10.1038/s41524-019-0265-1.

[39] Z. Pei, J. Yin, J.A. Hawk, D.E. Alman, M.C. Gao, Machine-learning informed prediction of high-entropy solid solution formation: Beyond the Hume-Rothery rules, Npj Comput. Mater. 6 (2020), https://doi.org/10.1038/s41524-020-0308-7.

[40] C. Zhang, J. Feng, L.R. DaCosta, P.M. Voyles, Atomic resolution convergent beam electron diffraction analysis using convolutional neural networks, Ultramicroscopy 210 (2020), 112921, https://doi.org/10.1016/j.ultramic.2019.112921.

[41] J. Madsen, P. Liu, J. Kling, J.B. Wagner, T.W. Hansen, O. Winther, J. Schiøtz, A Deep Learning Approach to Identify Local Structures in Atomic-Resolution Transmission Electron Microscopy Images, Adv. Theory Simulations. 1800037 (2018) 1800037, https://doi.org/10.1002/adts.201800037.

[42] M. Ragone, V. Yurkiv, B. Song, A. Ramsubramanian, R. Shahbazian-Yassar, F. Mashayek, Atomic column heights detection in metallic nanoparticles using deep convolutional learning, Comput. Mater. Sci. 180 (2020), 109722, https://doi.org/10.1016/j.commatsci.2020.109722.

[43] J. Miao, P. Ercius, S.J.L. Billinge, Atomic electron tomography: 3D structures without crystals, Science 353 (2016), https://doi.org/10.1126/science.aaf2157.

[44] G. Kresse, J. Furthmüller, Efficient iterative schemes for ab initio total-energy calculations using a plane-wave basis set, Phys. Rev. B 54 (16) (1996) 11169–11186, https://doi.org/10.1103/PhysRevB.54.11169.

[45] Atomistix Toolkit version 2017.2, Synopsys QuantumWise A/S.

[46] C. Ophus, A fast image simulation algorithm for scanning transmission electron microscopy, Adv. Struct. Chem. Imaging. 3 (2017) 1–11, https://doi.org/10.1186/s40679-017-0046-1.

[47] A.S.U. (2002). C. Koch, Ph.D. Thesis, PyQSTEM.

[48] M. Abadi, A. Agarwal, P. Barham, E. Brevdo, Z. Chen, C. Citro, G.S. Corrado, A. Davis, J. Dean, M. Devin, S. Ghemawat, I. Goodfellow, A. Harp, G. Irving, M. Isard, Y. Jia, R. Jozefowicz, L. Kaiser, M. Kudlur, J. Levenberg, D. Mane, R. Monga, S. Moore, D. Murray, C. Olah, M. Schuster, J. Shlens, B. Steiner, I. Sutskever, K. Talwar, P. Tucker, V. Vanhoucke, V. Vasudevan, F. Viegas, O. Vinyals, P. Warden, M. Wattenberg, M. Wicke, Y. Yu, X. Zheng, TensorFlow: Large-Scale Machine Learning on Heterogeneous Distributed Systems, ArXiv. (2016). http://arxiv.org/abs/1603.04467.

[49] J.H. Andrew Gibiansky, Bringing HPC Techniques to Deep Learning, (2017). https://andrew.gibiansky.com/blog/machine-learning/baidu-allreduce/.

[50] Tensorflow Mixed Precision, (n.d.). https://www.tensorflow.org/guide/mixed_precision.

[51] B.L. Gyorffy, G.M. Stocks, Concentration waves and Fermi surfaces in random metallic alloys, Phys. Rev. Lett. 50 (5) (1983) 374–377, https://doi.org/10.1103/PhysRevLett.50.374.